coatings

MDPI

Article

Controllable Synthesis of Nanostructured Ca-P Coating on Magnesium Alloys via Sodium Citrate Template-Assisted Hydrothermal Method and Its Corrosion Resistance

Jieling Wei [1], Shu Cai [1,*], Qianqian Li [1], Yao Xie [1], Xiaogang Bao [2] and Guohua Xu [2,*]

[1] Key Laboratory for Advanced Ceramics and Machining Technology of Ministry of Education, Tianjin University, Tianjin 300072, China; weijieling@tju.edu.cn (J.W.); liqianqian@tju.edu.cn (Q.L.); xieyao0726@tju.edu.cn (Y.X.)

[2] Department of Orthopedic Surgery, Spine Center, Changzheng Hospital, Naval Medical University, Shanghai 200003, China; bxg1832178@smmu.edu.cn

* Correspondence: caishu@tju.edu.cn (S.C.); xuguohuamail@smmu.edu.cn (G.X.)

Received: 5 November 2020; Accepted: 14 December 2020; Published: 16 December 2020

Abstract: In this study, a nanostructured needle-like hydroxyapatite (HA) coating was prepared by the sodium citrate template-assisted hydrothermal method on magnesium alloy (AZ31). The influence of sodium citrate on the composition, microstructure and corrosion behavior of the coatings was studied. The results showed that with the increase in the mole ratio of Ca/sodium citrate from 1 to 13, the coating gradually changed from the needle-like morphology of HA to the flake morphology of β-tricalcium phosphate (β-TCP), which was related to the existing form of citrate in the solution and the trend of complexation reaction. When the mole ratio of Ca/sodium citrate was 1, the HA coating sample with the nano needle-like morphology had a high corrosion resistance (R_t = 235.300 ± 3.584 kΩ·cm^2), which was almost 200 times that of the naked AZ31 alloy. Moreover, the corrosion rates of the Ca-P coated AZ31 alloy stabilized at about 0.55 mm/year and could provide more than 56 days of corrosion protection to the samples, which approximated the degradation rate requirement for biomaterials used as bone fixture.

Keywords: hydrothermal method; magnesium alloy; sodium citrate; corrosion resistance; hydroxyapatite

1. Introduction

Magnesium alloys have been receiving extensive attention and research-focus in the biomaterial field due to their excellent mechanical compatibility, biodegradability and biocompatibility. Nowadays, magnesium alloys are promising biomedical metallic materials in the field of orthopedics [1,2]. However, their rapid corrosion in the humoral environment can lead to a series of adverse effects [3,4], including the rapid deterioration failure of mechanical properties, local alkalization and severe hydrogen evolution reaction, which thus limits their clinical application [5].

Recent studies have shown that surface modifications by coatings prepared on magnesium alloys can improve corrosion resistance in the humoral environment effectively. There are some preparation methods that are usually used, such as the hydrothermal method [6–8], the sol–gel method [9–11], microwave treatment [12], chemical conversion treatment [13,14], micro-arc oxidation [15], anodization [16], plasma spraying [17], the dip coating method [18], electrophoretic deposition [19,20], the laser deposition technique [21], the biomimetic method [22], etc. Due to its lower temperature of reaction, making it easy to prepare dense and uniform coating, hydrothermal method is considered as one of the best ways to prepare coatings among these methods. [23]. Wang et al. [24] hydrothermally prepared MgAl hydrotalcite

conversion coating in situ on magnesium alloy, and Kaabi Falahieh Asl et al. [25] synthesized an intact and dense Ca-P coating on magnesium alloy substrates via the hydrothermal method, and both reduced the corrosion rates of the magnesium alloy substrate effectively. However, a single hydrothermal Ca-P coating is insufficient for bonding with the substrate [26]. It needs a middle layer which can provide a strong bond between the coating and the substrate, thereby having a longer corrosion protection effect on the substrate. Zhang et al. [27] synthesized a phytic acid conversion coating, which acted as the middle layer, and showed a high interface bonding strength between the hydroxyapatite coating and the magnesium alloy substrate.

In addition, the chemical composition is also an important factor influencing its corrosion resistance. It is well known that Ca and P are widely present in bone tissue. Recently, Ca-P coatings have attracted broad attention from of the researchers in the field of bone implant modification. The commonly used Ca-P coating components include HA, β-TCP, calcium hydrogen phosphate dihydrate ($CaHPO_4{\cdot}2H_2O$, CHPD), biological glass, etc. Li et al. [28] successfully prepared a dense and uniform HA coating on the surface of a polyvinyl alcohol (PVA)/polylactic acid (PLA) braid by electrodeposition. Yu et al. [29] characterized a nano-scale HA coating through the hydrothermal method on a pure titanium substrate, and revealed that the coating had a higher apatite-forming ability (bioactivity). Zhong et al. [30] synthesized a β-tricalcium phosphate coating on AZ31B alloy, proving that it can control the biodegradation rate of magnesium alloy AZ31B to some extent. Lin et al. [26] used the hydrothermal method to synthesize a Mg-doped β-TCP and magnesium hydroxide (β-TCMP/$Mg(OH)_2$) composite coating on AZ31 alloy. This coating has an adequate bonding strength and an extremely high impedance. Bakhsheshi-Rad et al. [31] prepared a CHPD coating on Mg-Ca alloy via the electrochemical deposition method, which had high corrosion resistance. Huang et al. [32] prepared mesoporous 58S bioactive glass (58S MBG) coatings via a sol-gel method, and proved that the coatings had great corrosion resistance and could induce the apatite precipitation on the surface.

In this work, Ca-P coatings are prepared on magnesium alloys (AZ31) via the sodium citrate-template assisted hydrothermal method, which are expected to act as promising corrosion resistant coatings on magnesium alloy in the humoral environment. The composition and microstructure, electrochemical properties and in vitro degradation of Mg alloy with Ca-P coatings and the mechanism of controllable synthesis by sodium citrate-template were investigated.

2. Materials and Methods

2.1. Substrate Pretreatment and Preparation

A magnesium alloy (AZ31) plate with has dimensions of 10 × 10 × 2 mm^3 was used as a substrate. The plates were mechanically polished with 400, 1200 and 2000 grit SiC papers successively, then ultrasonically washed in absolute ethanol for 3 min. After being dried at room temperature, these plates were treated in 1.5 M NaOH solution at 80 °C for 1 h. Next, the pretreated plates were cleaned by distilled water and absolute ethanol, then dried at room temperature for hydrothermal use.

The formulation of hydrothermal solution was as follows: different amounts of sodium citrate (according to Ca/sodium citrate mole ratios of 1, 4, 7, 10 and 13) were separately dissolved in 10 mL distilled water in five beakers, and 0.055 g $Ca(NO_3)_2{\cdot}4H_2O$ and 0.050 g $Na_2HPO_4{\cdot}12H_2O$ was dissolved in 40 mL and 50 mL of distilled water, respectively. The sodium citrate solution was instilled into $Ca(NO_3)_2$ solution with constant stirring, then the Na_2HPO_4 solution was instilled into the above $Ca(NO_3)_2$-sodium citrate mixed solution, and the pH values of the mixed solutions were adjusted to 5.50 [26] using 1 M HNO_3 solution. Afterwards, the pretreated AZ31 plates were immersed in the 50 mL autoclave with 35 mL of solution and then hydrothermally treated at 140 °C for 3 h. The obtained coatings using coating solutions with Ca/sodium citrate mole ratios from 1 to 13 were denoted successively as CN1, CN4, CN7, CN10 and CN13. Finally, these samples were rinsed with distilled water and absolute ethanol, and then dried at room temperature.

2.2. Phase Compositions and Microstructures

The phase compositions of the coated AZ31 magnesium alloys were investigated by X-ray diffraction (XRD, Rigaku D, Tokyo, Japan) with a scan step of 4°/min and an incidence angle of 3° over the 2θ range of 5°–70°. The surface and cross-section micro morphologies of the samples were characterized by field emission scanning electron microscopy (FE-SEM, S-4800, Hitachi, Japan) equipped with an energy dispersive spectrometer (EDS, X-Max20, Oxford, UK).

2.3. Electrochemical Test

The CHI660E electrochemical workstation (Shanghai Chenhua instrument Co., Shanghai, China) was used to quickly evaluate the electrochemical corrosion resistance of the samples. The following three-electrode system was used: extremely saturated calomel electrode as reference electrode, platinum electrode as counter electrode, and the tested samples as working electrode. Some treatment should be performed on the tested samples to make them usable working electrodes before the test: One corner of the samples was drilled, and the copper wires were fixed with the samples through the holes. The upper surface of the sample was the working face, while the rest of the surface and the copper wire were encapsulated with epoxy resin to keep the contact area between the working face and the corrosive medium at about 100 mm^2.

The samples were tested at 37 °C in simulated body fluid (SBF) [33]. First, they were soaked in SBF for at least 10 min to obtain a stable open circuit potential before the tests. Next, the electrochemical impedance spectroscopy (EIS) test was performed in a scan frequency ranging from 100 Hz to 0.01 Hz, and finally the scan rate was set to 1.0 mV/s to perform the potentiodynamic polarization test. At least three parallel samples were tested to guarantee reproducibility, and we took the average of the results as the final result.

2.4. In Vitro Immersion Tests

The in vitro immersion test is one of the important methods of to evaluating the long-term corrosion resistance of coatings. The samples were immersed in SBF at 37 °C by using a thermostat (FYLYS-150L, Beijing Fuyi instrument Co., Ltd., Beijing, China). The ratio of SBF volume to the working surface area of the samples was 20 mL/cm^2. The SBF solution was renewed every 2 days. The pH values of different samples of SBF were tested by the pH meter (PHS-25, Shanghai, China) at different immersion time nodes. Besides this, the soaked samples were taken out of SBF at the same time nodes. They were washed with chromic acid solution to remove coating, mineralized deposits, corrosion products and so on. from the sample surface, and then washed separately with distilled water and absolute ethanol, dried and weighed at room temperature. The corrosion rate of the sample was calculated by following Equation (1):

$$V_{corr} = (M_1 - M_2)/(S \times t \times \rho) \quad (1)$$

where V_{corr} represents the corrosion rate, M_1 represents the quality of the naked AZ31 alloy plate, M_2 represents the quality of the sample washed by chromic acid, S represents the surface area of the immersed sample, and t and ρ represent the immersion time and density of the AZ31 alloy, respectively. At least three parallel samples were tested and we took the average of their corrosion rate as a result.

3. Results and Discussion

3.1. Phase Composition and Microstructure of Ca-P Coatings

The composition and microstructure of the coating directly influence the corrosion behavior of the Mg alloy and its service in the humoral environment [34]. While we prepared coated samples by the sodium citrate template-assisted hydrothermal method, we found that the content of sodium citrate in the hydrothermal solution may influence the nucleation and growth of the Ca-P crystal, and this

was the important factor for Ca-P coating preparation. Therefore, based on the optimization of other experimental conditions [7,26], the influence of different contents of sodium citrate on the composition and microstructure of Ca-P coatings was mainly explored.

XRD patterns of the coatings prepared by the sodium citrate template-assisted hydrothermal method with different contents of sodium citrate were shown in Figure 1. All five coated samples consisted of magnesium (Mg, JCPDS # 65-3365), magnesium hydroxide ($Mg(OH)_2$, JCPDS # 76-0667), β-TCP (JCPDS # 70-2065) and HA (JCPDS # 74-0565). The diffraction patterns of $Mg(OH)_2$ indicate that the $Mg(OH)_2$ layer was formed on the surface of each AZ31 substrate, then different Ca-P coatings were successfully prepared when the mole ratios of Ca/sodium citrate in the hydrothermal solution were 1, 4, 7, 10 and 13, respectively. However, the intensity of the diffraction patterns for these samples appeared significantly different. From the samples CN1 to CN13, the relative diffraction peak intensity of HA was decreased gradually until it disappeared, and this simultaneously accompanied the increasing of the diffraction peak intensity of β-TCP simultaneously. It can be speculated that the Ca-P coating was transformed from HA to β-TCP, while the content of sodium citrate was decreased.

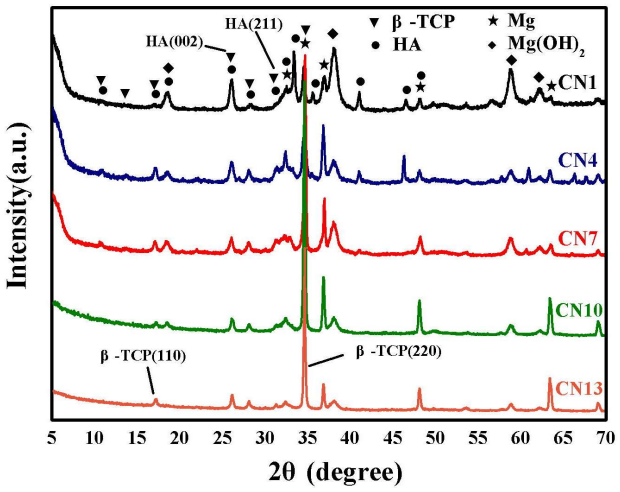

Figure 1. X-ray diffraction (XRD) patterns of the Ca-P-coated samples prepared at different contents of sodium citrate.

All five coated samples had diffraction peaks of Mg. The intensity of Mg peaks was increased from CN1 to CN10; however, with the decreasing of the sodium citrate content, the Mg peak's intensity in CN13 was decreased however. Meanwhile, compared to the standard diffraction peak of HA and β-TCP, the diffraction peak position of HA was shifted about 0.3° to the right, and the peaks of β-TCP shifted by 0.1° to higher angle values, respectively, demonstrating that the thickness of coatings decreased from CN1 to CN10 and slightly increased up to CN13, and Mg^{2+} was doped into Ca-P coatings simultaneously (proved by Table 1). For CN1, the diffraction peak intensity of the HA (002) crystal plane was much higher than HA (211), indicating that the HA crystal tended to grow in the direction of the *c*-axis. From samples CN4 to CN13, the diffraction peak intensities of the (110) and (220) crystal plane of β-TCP were increased obviously, demonstrating that the β-TCP crystals grew into lamellar structures, and their crystallinity was high.

Figure 2 provides the surface morphologies of the naked AZ31 alloy and the Ca-P-coated samples prepared at different contents of sodium citrate. It is shown that the surface of the naked AZ31 alloy exhibited a number of scratches that took place during the mechanical polishing process (Figure 2a). After the hydrothermal process at different amount of sodium citrate in the solution, there were distinct changes in the microstructures and the components of the surfaces of the AZ31 substrates.

Table 1. Element composition of area A, B, C, D, E, F, G and H in Figure 2.

Element	Atomic Concentration (%)							
	Area A	**Area B**	**Area C**	**Area D**	**Area E**	**Area F**	**Area G**	**Area H**
C	12.2	8.1	11.8	6.7	10.6	14.8	13.0	15.2
O	25.9	61.2	54.4	33.1	55.5	47.5	44.6	49.0
Mg	3.4	4.0	2.8	9.0	3.5	6.6	3.2	2.7
Ca	35.9	16.4	17.6	31.3	17.2	18.3	22.3	18.4
P	22.6	10.2	13.3	19.9	13.2	12.8	16.9	14.8

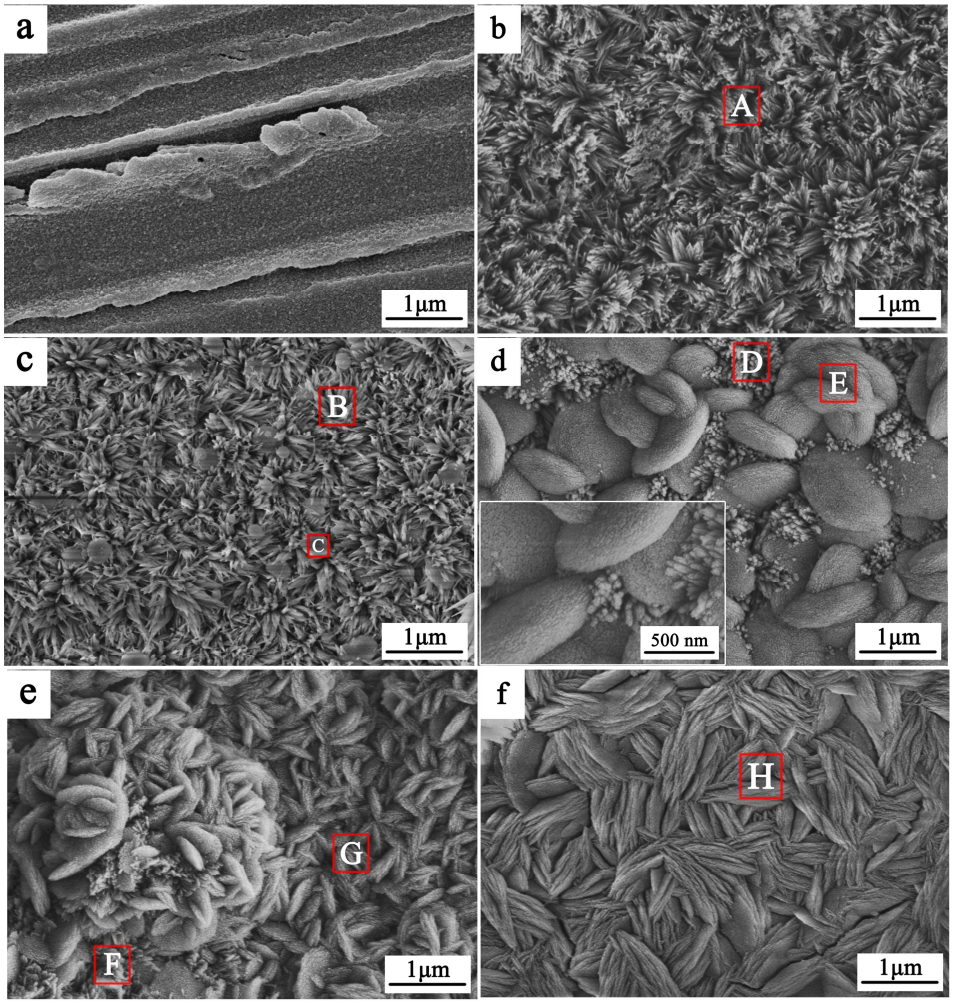

Figure 2. Surface morphologies of (**a**) naked AZ31 alloy; (**b**) CN1; (**c**) CN4; (**d**) CN7; (**e**) CN10; (**f**) CN13.

A uniform and compact coating was prepared on magnesium for sample CN1, which consisted of nano-needle-like crystals (Figure 2b). The elemental composition was analyzed by EDS (Table 1). The ratio of (Ca + Mg)/P in the coating (area A) was 1.74, which was close to that of stoichiometric HA (1.67), demonstrating that the composition of the CN1 coating was Mg-doped HA. Figure 3 shows the cross-sectional SEM microstructure of CN1 and the elements' distribution curves (Mg, O, Ca, P) for the coating by using line scanning EDS analysis. The $Mg(OH)_2$ layer, with a thickness of 20.9 μm, was observed on the surface of the AZ31 alloy substrate, and a uniform and dense Mg-doped HA coating with a thickness of 9.8 μm was covered on it, the microstructure of which was consistent with the XRD analysis mentioned above. It can be observed through SEM that the $Mg(OH)_2$ layer and the Mg-doped HA coating of CN1 were still tightly bound without any defects after grinding and polishing, indicating that the CN1 coating was well bonded to the substrate. Besides this, the surface of

the AZ31 substrate was kept flat, and the $Mg(OH)_2$ layer had no defects and was of uniform thickness, demonstrating that the substrate would not be damaged during the preparation process.

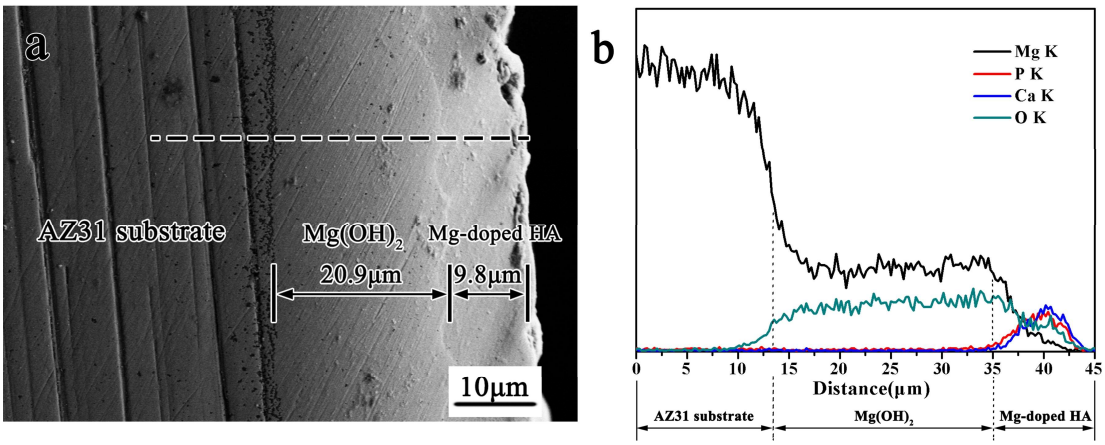

Figure 3. (**a**) The cross-sectional microstructure of CN1. (**b**) The elements' distribution along the dotted line in Figure 3a.

With the decrease in the concentration of sodium citrate in the hydrothermal solution, spherical aggregates with a diameter of 200–600 nm appeared on the coating of CN4. The spherical aggregates on the CN7 coating grew up to leather-like ellipsoids, the long axes of which were about 1–1.25 μm, and the short axes were about 300–500 nm, while the needle-like crystals were significantly reduced. For the CN10, the long and short axes of the leather-like ellipsoidal aggregates were observably reduced, and the ellipsoidal aggregates had the trend of separation to the plate crystals. Finally, the coating surface of CN13, as shown in Figure 2f, was evenly covered by the plate crystals, and the needle-like crystals disappeared completely.

The elemental compositions of the other samples different areas were also summarized in Table 1. It could be seen that all the coatings contained Ca, Mg, O and P. The (Ca + Mg)/P ratio for the coating crystals with different morphologies changed greatly. The ratios of (Ca + Mg)/P in the areas A, B, D and F, which consisted of needle-like crystals, were 1.74, 2.00, 2.03 and 1.95, respectively, and the corresponding Ca/P ratios were 1.59, 1.61, 1.57 and 1.43, while the Mg/P ratio was increased by 0.15, 0.39, 0.45 and 0.53, respectively. The CN1 coating was consisted of Mg-doped HA. It was speculated that from CN4 to CN10, with the increase in Mg content in the coating, excessive Mg^{2+} was doped into the HA lattice, resulting in the destruction of the HA crystal structure. Therefore, it is conjectured that the crystallinity of HA in the regions B, D and F decreased and its properties became more unstable. Moreover, the ratios of (Ca + Mg)/P for spherical aggregates, leather-like ellipsoidal aggregates and plate crystals corresponding to C, E(G) and H were in the range of 1.43–1.57, which is approximately that of stoichiometric β-TCP (1.5), indicating that the composition of these areas was Mg-doped β-TCP. It can be seen from the intensity of the diffraction pattern for the (220) peak of β-TCP in Figure 1 that the peak intensity of CN4 was only slightly higher than that of CN1, while the peak intensity of CN7 increased sharply. In combination with Figure 2 and the above analysis, it could be inferred that the spherical aggregates in CN4 were β-TCP with low crystallinity, and in the CN7 sample coating, the crystallinity of β-TCP was significantly improved and transformed into leathery ellipsoid aggregates formed by strip-like crystals with a thickness of about 10 nm. From CN7 to CN13, the β-TCP ellipsoids were separated layer by layer and gradually changed into a lamellae structure.

The above results shown that the nucleation and the growth of the Ca-P compounds were tightly associated with the content of sodium citrate in the template-assisted hydrothermal method. The sodium citrate dissolved into H_2O and ionized into Na^+ and Cit^{3-} (Figure 4a), while the Cit^{3-} in solution occurred via the hydrolysis/ionization equilibrium reaction, and the final main form was

related to the pH value of the solution. The relationship between the percentages of citrate in the different forms and the pH are was shown in Figure 4b [35].

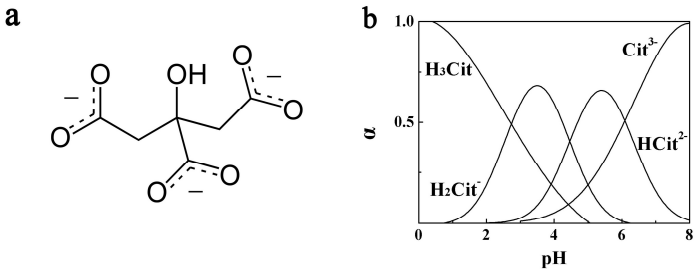

Figure 4. Some information of citrate. (**a**) Two−dimensional formula of citrate. (**b**) Distribution diagram of the citric forms when the pH value changes.

While the sodium citrate solution was mixed with the calcium nitrate solution in this study, the pH value of the mixed solution was about 4.0. At this time, the citrate mainly existed in the form of H_2Cit^-. H_2Cit^- bound closely with Ca^{2+} in the solution in a 1:1 ratio to form the complex group $[Ca^{2+}H_2Cit^-]^+$. The $Mg(OH)_2$ coating acted as a kind of protective layer, which was prepared on the AZ31 alloy substrate surface during the alkali treatment, and could effectively prevent the substrate from directly contacting with the solution at the initial stage of the hydrothermal reaction. Furthermore, the $Mg(OH)_2$ coating was a conversion coating, and it could provide the –OH, which usually acted as a nucleation site for the deposition of Ca-P compounds [33,36].

After mixing all solution and adjusting the pH value to 5.5, for sample CN1 (Figure 5a), at the beginning of hydrothermal process, the $[Ca^{2+}H_2Cit^-]^+$ and $Mg(OH)_2$ layer combined through an hydrogen bond between –OHs. As such, the $[Ca^{2+}H_2Cit^-]^+$ covered the entire surface quickly. At the same time, $[Ca^{2+}H_2Cit^-]^+$ ionized to $[Ca^{2+}HCit^{2-}]$v and generated H^+, and the $Mg(OH)_2$ layer began to degraded slightly. However, the radius size of Mg^{2+} was smaller than Ca^{2+}, so that Mg^{2+} could form stronger coordination bonds with the citrate because of its higher electronegativity. Therefore, Mg^{2+} was more easily complexed to citrate than Ca^{2+}. In this study, the $–COO^-$ which was ionized by the complex group $[Ca^{2+}H_2Cit^-]^+$ was easily complexed to Mg^{2+}, resulting in a stronger bond between the citrate and the $Mg(OH)_2$ layer. In addition, the citrate did not decompose at 140 °C, so the complex group was still positively charged and could adsorb PO_4^{3-} and OH^-. Under the action of hydrothermal action, a stable HA crystal nucleus is formed on the surface, and then grew along the c axis because of the existence of citrate [37], and then finally formed a nanoneedle-like morphology.

As regards the other Ca-P-coated samples (Figure 5b), the partial Ca^{2+} remained free after complexation with H_2Cit^- to form $[Ca^{2+}H_2Cit^-]^+$ in the solution, while the sodium citrate solution was mixed with the calcium nitrate solution. Lin et al. [26] proved that the solution containing sufficient concentrations of Ca^{2+} and PO_4^{3-} ions tends to form β-TCP at 140 °C of hydrothermal heating when the pH value is 5.5 and sodium citrate is not added. Moreover, the doping of Mg^{2+} would help to form Mg-doped β-TCP, which has lower solubility and stable properties [38]. In this study, with the decrease in the concentration of sodium citrate in the solution, $[Ca^{2+}H_2Cit^-]^+$ could not evenly cover the whole surface of the $Mg(OH)_2$ layer at the beginning of the hydrothermal process. The $Mg(OH)_2$ layer was directly exposed to acidic solution and degraded rapidly at the region lacking $[Ca^{2+}H_2Cit^-]^+$. The –OH on the surface of the $Mg(OH)_2$ layer after degradation electrostatically attracted the free Ca^{2+}, then the Ca^{2+} attracted PO_4^{3-} deposition, thus forming β-TCP in this region. Due to the degradation of the $Mg(OH)_2$ layer, more Mg^{2+} was released into the hydrothermal solution. On the one hand, Mg^{2+} influenced the β-TCP area, and made it transform into a more stable flake Mg-doped β-TCP. On the other hand, excess Mg^{2+} was doped into the HA lattice and destroyed the crystal structure of HA, making the HA's crystallinity and stability decrease, consistent with the EDS analysis results.

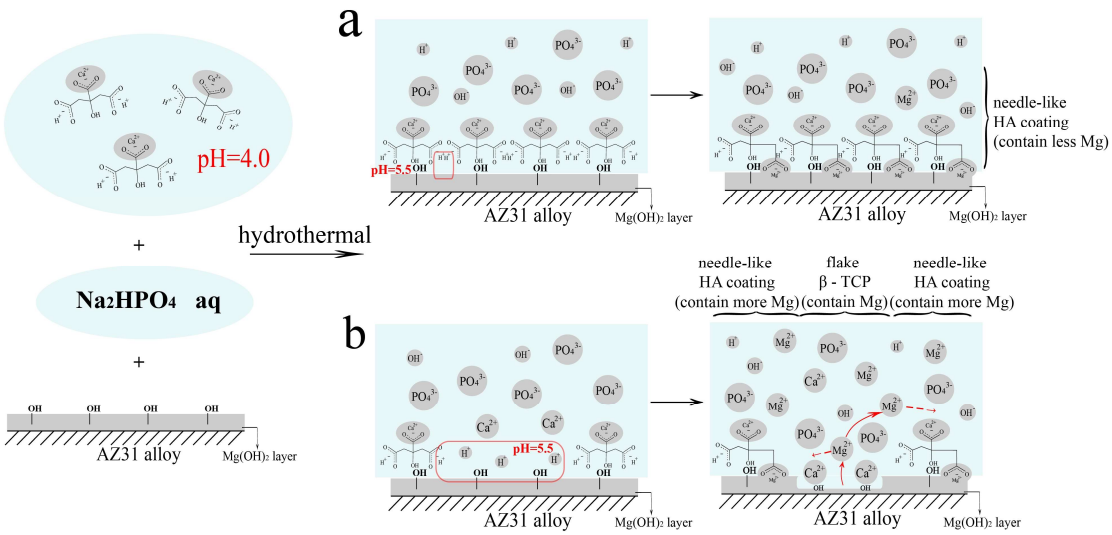

Figure 5. Schematic illustrations showing the sodium citrate control mechanisms of Ca-P coating. (**a**) CN1; (**b**) CN4-CN13.

3.2. Corrosion Resistance of Ca-P Coatings

In order to quickly evaluate the effects of different sodium citrate contents on the corrosion resistance of Ca-P coatings, a series of electrochemical tests was implemented for the naked Mg alloy and the Ca-P-coated samples (CN1, CN4, CN7, CN10 and CN13) in the SBF solution. The results are shown in Figure 6.

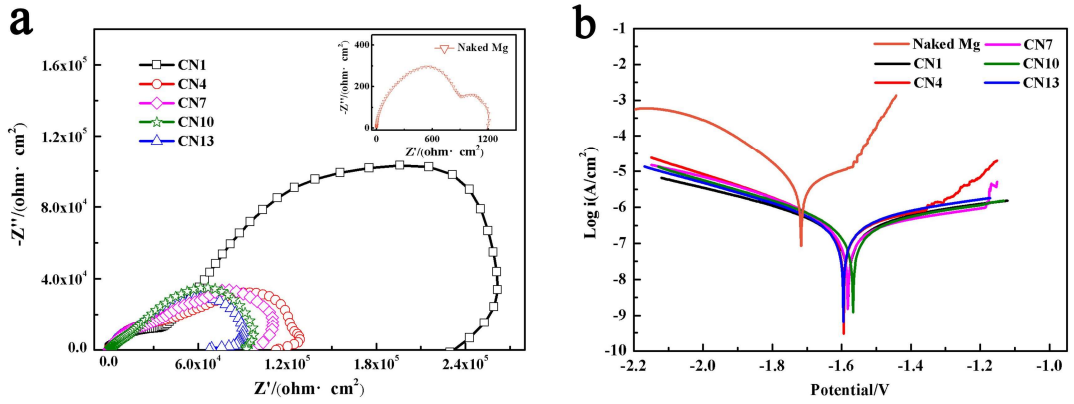

Figure 6. Electrochemical properties of the naked Mg alloy and different Ca-P-coated samples in SBF solution: (**a**) Nyquist plots; (**b**) potentiodynamic polarization curves.

The results of the EIS measurement are shown in Figure 6a. According to the study in Ref. [39], the capacitive reactance arc in the high frequency range was ascribed to the charge transfer reaction, and the capacitive reactance arc in the range of intermediate frequency was attributed to the mass transfer of the corrosion products. The presence of the intermediate frequency capacitive reactance arc means that the Mg substrate has been eroded by the corrosive electrolyte. Therefore, the naked Mg alloy samples' results (the insert in Figure 6a) show that the small capacitating resistance arc in the high frequency range was attributed to the corrosion protection effect of the loose oxide film, while the apparent low capacitive resistance arc in the medium frequency range reflects that the AZ31 substrate had contacted the SBF solution and the corrosion reaction occurred. The EIS curves of the CN1 samples had only one capacitive reactance arc, while some of the other Ca-P-coated samples showed very small capacitive reactance arcs in the range of the medium frequency, indicating that the CN1 coating had a good protective effect on the substrate, and the other Ca-P coated samples experienced a slight

corrosion reaction. In addition, the diameter of the capacitive reactance arc was usually used as the charge transfer resistance (R_t). The larger this value was, the higher the electrochemical corrosion resistance of the material would be [27,40]. In this study, the R_t values of each sample (Table 2) were CN1 > CN4 > CN7 > CN10 > CN13 > naked AZ31 alloy in descending order, indicating that the Ca-P coating prepared with a Ca/sodium citrate concentration ratio of 1 had better corrosion resistance. Meanwhile, the Rt value of CN1 is about 195 times that of naked AZ31 alloy, demonstrating that the coating has a good electrochemical corrosion protection effect and can effectively isolate the magnesium alloy substrate from the external corrosive medium.

Table 2. Electrochemical properties of the naked Mg alloy and different Ca-P-coated samples.

Samples	R_t (kΩ·cm^2)	i_{corr} (μA/cm^2)	E_{corr} (V/SCE)
Naked Mg	1.195 ± 0.045	13.280 ± 1.658	−1.713 ± 0.017
CN1	235.300 ± 3.584	0.156 ± 0.023	−1.582 ± 0.012
CN4	112.100 ± 3.218	0.201 ± 0.034	−1.594 ± 0.013
CN7	99.810 ± 3.196	0.161 ± 0.029	−1.582 ± 0.013
CN10	97.610 ± 3.187	0.171 ± 0.032	−1.567 ± 0.014
CN13	68.090 ± 3.083	0.207 ± 0.040	−1.595 ± 0.012

Besides this, the corrosion resistance of the samples could also be evaluated via the potentiodynamic polarization test (Figure 6b). The corrosion potential (E_{corr}) and corrosion current density (i_{corr}) were obtained by using the tafel extrapolation method and summarized in Table 2. The lower values of i_{corr} indicate that the coatings have a better protective ability for the AZ31 alloy substrates [27]. Compared with the naked Mg, the i_{corr} of Ca-P-coated samples decreased by two orders of magnitude, and the i_{corr} of CN1 was the lowest. Therefore, the CN1 with the lowest i_{corr} value and the highest R_t value had the best corrosion resistance among these samples. Its coating could effectively prevent the penetration of the SBF solution, and it provided good protection for the AZ31 substrate.

For the further study of the corrosion resistance of Ca-P coatings prepared with different contents of sodium citrate, all six samples were immersed in SBF for the in vitro immersion test to observe the long-term corrosion resistance behavior. The SBF solution's pH variation (of the control group of naked AZ31 alloy and Ca-P coated samples) and the average corrosion rate of Ca-P-coated samples after immersion are given in Figure 7a,b, respectively.

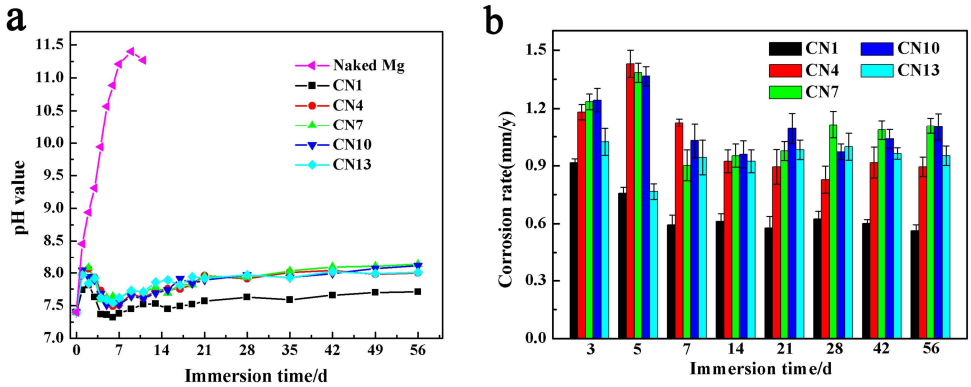

Figure 7. Different Ca-P coating samples (and naked AZ31 alloy) after immersion in SBF for different time nodes: (**a**) pH values of SBF solution; (**b**) average corrosion rates.

The pH value of SBF with naked AZ31 alloy increased rapidly and reached up to 11 in the first 7 days (Figure 7a). The study had shown that Mg could be reacted in an aqueous solution such as SBF, and generates OH^- to alkalize the solution, and then the Cl^- in the solution converts the loose layer which is composed of corrosion products, accelerating the release of OH^- and leading to the rapid corrosion of the magnesium alloy [41]. After 11 days of immersion, the naked AZ31 alloy was

almost completely degraded. However, the five Ca-P-coated samples kept their original macroscopic shape after soaking for 56 days. Among the five Ca-P-coated samples, the SBF solution with the CN1 sample presented the lowest pH values (under 7.70) during the entire immersion period. The pH values of the SBF solutions of other Ca-P coating samples were higher than those of the CN1 samples, remaining at about 8.0 after 56 days of immersion, demonstrating that the CN1 coating could provide better sufficient protection to the AZ31 substrates from the corrosion by SBF.

For more quantitative assessment, the corrosion rates of the Ca-P coating samples are shown in Figure 7b. These showed that the corrosion rates of the CN1 samples stayed below 1 mm/year during the whole immersing process, and finally it stabilized at about 0.55 mm/year, which was closed to the degradation rate requirement of less than 0.5 mm/year in the SBF solution for bone implant biomaterials [1]. However, the corrosion rates of the other Ca-P coating samples were significantly higher than that of CN1 sample, and finally stabilized above 0.9 mm/year.

In combination with the above analysis, the CN1 sample was the one with the best performance in all the Ca-P coated samples.

4. Conclusions

In this study, different kinds of nanostructured Ca-P coatings were prepared on AZ31 alloy via the sodium citrate template-assisted hydrothermal method. The amount of sodium citrate template could control the composition and morphology of the coatings. With the decrease in sodium citrate, the coating gradually changed from the needle-like morphology of HA to the flake morphology of β-TCP, which was related to the existing form of citrate in solution and the trend of the complexation reaction. In all the Ca-P coating samples, the CN1 sample whose molar ratio of Ca and sodium citrate was 1 had a higher charge transfer resistance (235.300 ± 3.584 $k\Omega \cdot cm^2$) and a lower corrosion current density (0.156 ± 0.023 $\mu A/cm^2$), indicating that it had effective electrochemical corrosion resistance. The immersion test of the CN1 sample in SBF showed that the CN1 coating on the surface could provide protection for the AZ31 magnesium alloy substrate for more than 56 days, and the corrosion rates of it stabilized at about 0.55 mm/year, which approximated the degradation rate requirement of biomaterials used as bone fixtures. Consequently, the sodium citrate template-assisted hydrothermal method could control the composition and microstructure of Ca-P coatings on an AZ31 alloy substrate. The needle-like CN1 coating sample among them was an effective surface modified coating for biomedical AZ31 alloy, used to improve the long-term corrosion resistance.

Author Contributions: Conceptualization, S.C. and X.B.; funding acquisition, S.C.; methodology, Q.L.; project administration, G.X.; resources, X.B. and G.X.; software, Y.X.; supervision, Y.X.; validation, Q.L.; writing—original draft, J.W.; writing—review & editing, J.W. All authors have read and agreed to the published version of the manuscript.

Funding: The work was financially supported by the National Natural Science Foundation of China (grant Number 51872197, 51572186 and 81772363) and Shanghai Committee of Science and Technology, China (grant number. 15411951000).

Conflicts of Interest: The authors declare no conflict of interest.

References

1. Chen, Y.; Xu, Z.; Smith, C.; Sankar, J. Recent advances on the development of magnesium alloys for biodegradable implants. *Acta Biomater.* **2014**, *10*, 4561–4573. [CrossRef] [PubMed]
2. Zhao, D.; Feyerabend, F.; Lu, F.; Wang, J.; Jiali, W.; Qin, L. Current status on clinical applications of magnesium-based orthopaedic implants: A review from clinical translational perspective. *Biomaterials* **2017**, *112*, 287–302. [CrossRef] [PubMed]
3. Song, G. Control of biodegradation of biocompatable magnesium alloys. *Corros. Sci.* **2007**, *49*, 1696–1701. [CrossRef]
4. Tan, L.; Wang, Q.; Lin, X.; Wan, P.; Zhang, G.; Zhang, Q.; Yang, K. Loss of mechanical properties in vivo and bone-implant interface strength of AZ31B magnesium alloy screws with Si-containing coating. *Acta Biomater.* **2014**, *10*, 2333–2340. [CrossRef]

5. Huang, W.; Xu, B.; Yang, W.; Zhang, K.; Chen, Y.; Yin, X.; Liu, Y.; Ni, Z.; Pei, F. Corrosion behavior and biocompatibility of hydroxyapatite/magnesium phosphate/zinc phosphate composite coating deposited on AZ31 alloy. *Surf. Coat. Technol.* **2017**, *326*, 270–280. [CrossRef]
6. Onoki, T.; Yamamoto, S.; Onodera, H.; Nakahira, A. New technique for bonding hydroxyapatite ceramics and magnesium alloy by hydrothermal hot-pressing method. *Mater. Sci. Eng. C* **2011**, *31*, 499–502. [CrossRef]
7. Li, Y.; Shen, S.; Zhu, L.; Cai, S.; Jiang, Y.; Ling, R.; Jiang, S.; Lin, Y.; Hua, S.; Xu, G. In vitro degradation and mineralization of strontium-substituted hydroxyapatite coating on magnesium alloy synthesized via hydrothermal route. *J. Ceram. Soc. Jpn.* **2019**, *127*, 158–164. [CrossRef]
8. Song, D.; Guo, G.; Jiang, J.; Zhang, L.; Ma, A.; Ma, X.; Chen, J.; Cheng, Z. Hydrothermal synthesis and corrosion behavior of the protective coating on Mg-2Zn-Mn-Ca-Ce alloy. *Prog. Nat. Sci. Mater. Int.* **2016**, *26*, 590–599. [CrossRef]
9. Zhao, H.; Cai, S.; Niu, S.; Zhang, R.; Wu, X.; Xu, G.; Ding, Z. The influence of alkali pretreatments of AZ31 magnesium alloys on bonding of bioglass-ceramic coatings and corrosion resistance for biomedical applications. *Ceram. Int.* **2015**, *41*, 4590–4600. [CrossRef]
10. Jiang, Y.; Zhu, L.; Cai, S.; Shen, S.; Li, Y.; Jiang, S.; Lin, Y.; Hua, S.; Ling, R.; Xu, G. Corrosion-resistant fluoridated Ca-Mg-P composite coating on magnesium alloys prepared via hydrothermal assisted sol-gel process. *J. Mater. Res.* **2018**, *33*, 3793–3800. [CrossRef]
11. Han, J.; Yu, Z.; Zhou, L. Hydroxyapatite/titania composite bioactivity coating processed by sol-gel method. *Appl. Surf. Sci.* **2008**, *255*, 455–458. [CrossRef]
12. Jiang, S.; Cai, S.; Zhang, F.; Xu, P.; Ling, R.; Li, Y.; Jiang, Y.; Xu, G. Synthesis and characterization of magnesium phytic acid/apatite composite coating on AZ31 Mg alloy by microwave assisted treatment. *Mater. Sci. Eng. C Mater. Biol. Appl.* **2018**, *91*, 218–227. [CrossRef] [PubMed]
13. Liu, B.; Zhang, X.; Xiao, G.-Y.; Lu, Y.-P. Phosphate chemical conversion coatings on metallic substrates for biomedical application: A review. *Mater. Sci. Eng. C* **2015**, *47*, 97–104. [CrossRef] [PubMed]
14. Zhang, L.; Pei, J.; Wang, H.; Shi, Y.; Niu, J.; Yuan, F.; Huang, H.; Zhang, H.; Yuan, G. Facile Preparation of Poly(lactic acid)/Brushite Bilayer Coating on Biodegradable Magnesium Alloys with Multiple Functionalities for Orthopedic Application. *ACS Appl. Mater. Interfaces* **2017**, *9*, 9437–9448. [CrossRef] [PubMed]
15. Nan, K.; Wu, T.; Chen, J.; Jiang, S.; Huang, Y.; Pei, G. Strontium doped hydroxyapatite film formed by micro-arc oxidation. *Mater. Sci. Eng. C* **2009**, *29*, 1554–1558. [CrossRef]
16. Mousa, H.M.; Lee, D.H.; Park, C.H.; Kim, C.S. A novel simple strategy for in situ deposition of apatite layer on AZ31B magnesium alloy for bone tissue regeneration. *Appl. Surf. Sci.* **2015**, *351*, 55–65. [CrossRef]
17. Wang, Y.; Liu, X.; Fan, T.; Tan, Z.; Zhou, Z.; He, D. In vitro evaluation of hydroxyapatite coatings with (002) crystallographic texture deposited by micro-plasma spraying. *Mater. Sci. Eng. C Mater. Biol. Appl.* **2017**, *75*, 596–601. [CrossRef]
18. Predoi, D.; Iconaru, S.L.; Predoi, D. Fabrication of Silver- and Zinc-Doped Hydroxyapatite Coatings for Enhancing Antimicrobial Effect. *Coatings* **2020**, *10*, 905. [CrossRef]
19. Qi, H.; Heise, S.; Li, Q.; Schuhladen, K.; Yang, Y.; Cui, N.; Dong, R.; Virtanen, S.; Chen, Q.; Boccaccini, A.R.; et al. Electrophoretic Deposition of Bioadaptive Drug Delivery Coatings on Magnesium Alloy for Bone Repair. *ACS Appl. Mater. Interfaces* **2019**, *11*, 8625–8634. [CrossRef]
20. Yan, Y.; Dong, Q.; Huang, Y.; Han, S.; Pang, X. Magnesium substituted hydroxyapatite coating on titanium with nanotublar TiO_2 intermediate layer via electrochemical deposition. *Appl. Surf. Sci.* **2014**, *305*, 77–85. [CrossRef]
21. Boanini, E.; Torricelli, P.; Sima, F.; Axente, E.; Fini, M.; Mihailescu, I.N.; Bigi, A. Gradient coatings of strontium hydroxyapatite/zinc beta-tricalcium phosphate as a tool to modulate osteoblast/osteoclast response. *J. Inorg. Biochem.* **2018**, *183*, 1–8. [CrossRef] [PubMed]
22. Lin, B.; Zhong, M.; Zheng, C.; Cao, L.; Wang, D.; Wang, L.; Liang, J.; Cao, B. Preparation and characterization of dopamine-induced biomimetic hydroxyapatite coatings on the AZ31 magnesium alloy. *Surf. Coat. Technol.* **2015**, *281*, 82–88. [CrossRef]
23. Wu, G.; Ibrahim, J.M.; Chu, P.K. Surface design of biodegradable magnesium alloys—A review. *Surf. Coat. Technol.* **2013**, *233*, 2–12. [CrossRef]
24. Wang, L.; Zhang, K.; Sun, W.; Wu, T.; He, H.; Liu, G. Hydrothermal synthesis of corrosion resistant hydrotalcite conversion coating on AZ91D alloy. *Mater. Lett.* **2013**, *106*, 111–114. [CrossRef]

25. Asl, S.K.F.; Nemeth, S.; Tan, M.J. Hydrothermally deposited protective and bioactive coating for magnesium alloys for implant application. *Surf. Coat. Technol.* **2014**, *258*, 931–937. [CrossRef]
26. Lin, Y.; Cai, S.; Jiang, S.; Xie, D.; Ling, R.; Sun, J.; Wei, J.; Shen, K.; Xu, G. Enhanced corrosion resistance and bonding strength of Mg substituted beta-tricalcium phosphate/$Mg(OH)_2$ composite coating on magnesium alloys via one-step hydrothermal method. *J. Mech. Behav. Biomed. Mater.* **2019**, *90*, 547–555. [CrossRef] [PubMed]
27. Zhang, M.; Cai, S.; Shen, S.; Xu, G.; Li, Y.; Ling, R.; Wu, X. In-situ defect repairing in hydroxyapatite/phytic acid hybrid coatings on AZ31 magnesium alloy by hydrothermal treatment. *J. Alloys Compd.* **2016**, *658*, 649–656. [CrossRef]
28. Li, T.-T.; Ling, L.; Lin, M.-C.; Jiang, Q.; Lin, J.-H.; Lin, J.-H.; Lou, C.-W. Properties and Mechanism of Hydroxyapatite Coating Prepared by Electrodeposition on a Braid for Biodegradable Bone Scaffolds. *Nanomaterial* **2019**, *9*, 679. [CrossRef]
29. Yu, H.-N.; Hsu, H.-C.; Wu, S.-C.; Hsu, C.-W.; Wu, S.-C.; Ho, W.-F. Hsu Characterization of Nano-Scale Hydroxyapatite Coating Synthesized from Eggshells Through Hydrothermal Reaction on Commercially Pure Titanium. *Coatings* **2020**, *10*, 112. [CrossRef]
30. Zhong, L.-F.; Li, H.-Y.; Wang, T.-X.; Ren, B.; Wang, H.-Y. Experimental study on effects of fluoride and coating on the degradation behavior of magnesium alloy AZ31B in vitro. *J. Zhongguo Shiyong Kouqiangke Zazhi* **2012**, *5*, 350–353.
31. Bakhsheshi-Rad, H.; Hamzah, E.; Daroonparvar, M.; Ebrahimi-Kahrizsangi, R.; Medraj, M. In-vitro corrosion inhibition mechanism of fluorine-doped hydroxyapatite and brushite coated Mg–Ca alloys for biomedical applications. *Ceram. Int.* **2014**, *40*, 7971–7982. [CrossRef]
32. Huang, K.; Cai, S.; Xu, G.; Ren, M.; Wang, X.; Zhang, R.; Niu, S.; Zhao, H. Sol–gel derived mesoporous 58S bioactive glass coatings on AZ31 magnesium alloy and in vitro degradation behavior. *Surf. Coat. Technol.* **2014**, *240*, 137–144. [CrossRef]
33. Shen, S.; Cai, S.; Li, Y.; Ling, R.; Zhang, F.; Xu, G.; Wang, F. Microwave aqueous synthesis of hydroxyapatite bilayer coating on magnesium alloy for orthopedic application. *Chem. Eng. J.* **2017**, *309*, 278–287. [CrossRef]
34. Sun, J.; Cai, S.; Wei, J.; Shen, K.; Ling, R.; Sun, J.; Liu, J.; Xu, G. Long-term corrosion resistance and fast mineralization behavior of micro-nano hydroxyapatite coated magnesium alloy in vitro. *Ceram. Int.* **2020**, *46*, 824–832. [CrossRef]
35. Alexander, A.; Alexander, A. *Citric Acid*; Springer International Publish: Cham, Switzerland, 2014; pp. 146–149.
36. Metoki, N.; Rosa, C.; Zanin, H.; Marciano, F.; Eliaz, N.; Lobo, A.O. Electrodeposition and biomineralization of nano-β-tricalcium phosphate on graphenated carbon nanotubes. *Surf. Coat. Technol.* **2016**, *297*, 51–57. [CrossRef]
37. Delgado-López, J.M.; Frison, R.; Cervellino, A.; Gómez-Morales, J.; Guagliardi, A.; Masciocchi, N. Crystal Size, Morphology, and Growth Mechanism in Bio-Inspired Apatite Nanocrystals. *Adv. Funct. Mater.* **2013**, *24*, 1090–1099. [CrossRef]
38. Li, X.; Ito, A.; Sogo, Y.; Wang, X.; LeGeros, R.Z. Solubility of Mg-containing beta-tricalcium phosphate at 25 degrees C. *Acta Biomater.* **2009**, *5*, 508–517. [CrossRef]
39. Jamesh, M.; Kumar, S.; Narayanan, T.S. Electrodeposition of hydroxyapatite coating on magnesium for biomedical applications. *J. Coat. Technol. Res.* **2011**, *9*, 495–502. [CrossRef]
40. Ren, M.; Cai, S.; Liu, T.; Huang, K.; Wang, X.; Zhao, H.; Niu, S.; Zhang, R.; Wu, X. Calcium phosphate glass/MgF2 double layered composite coating for improving the corrosion resistance of magnesium alloy. *J. Alloys Compd.* **2014**, *591*, 34–40. [CrossRef]
41. Agarwal, S.; Curtin, J.; Duffy, B.; Jaiswal, S. Biodegradable magnesium alloys for orthopaedic applications: A review on corrosion, biocompatibility and surface modifications. *Mater. Sci. Eng. C Mater. Biol. Appl.* **2016**, *68*, 948–963. [CrossRef]